Ultra-Wideband SAR Tomography on Asteroids

Oriane Gassot, Alain Herique, Wenzhe Fa, Jun Du, Wlodek Kofman

▶ **To cite this version:**

Oriane Gassot, Alain Herique, Wenzhe Fa, Jun Du, Wlodek Kofman. Ultra-Wideband SAR Tomography on Asteroids. Radio Science, 2021, 56, ⟨10.1029/2020RS007186⟩. ⟨insu-03705284⟩

HAL Id: insu-03705284

https://insu.hal.science/insu-03705284v1

Submitted on 19 Aug 2022

HAL is a multi-disciplinary open access archive for the deposit and dissemination of scientific research documents, whether they are published or not. The documents may come from teaching and research institutions in France or abroad, or from public or private research centers.

L'archive ouverte pluridisciplinaire **HAL**, est destinée au dépôt et à la diffusion de documents scientifiques de niveau recherche, publiés ou non, émanant des établissements d'enseignement et de recherche français ou étrangers, des laboratoires publics ou privés.

Copyright - All rights reserved

Check for updates

Radio Science

RESEARCH ARTICLE
10.1029/2020RS007186

Key Points:

- High-Frequency Radar (HFR) is an UWB Synthetic Aperture Radar (SAR) developed to retrieve the 3D structure of the first 10 m of an asteroid's subsurface
- SAR Tomography (TomoSAR) is crucial to improve the resolution in the vertical direction
- In the specific asteroid geometry, simulations are necessary the assess the performances of the TomoSAR algorithms

Correspondence to:
O. Gassot,
oriane.gassot@univ-grenoble-alpes.fr

Citation:
Gassot, O., Herique, A., Fa, W., Du, J., & Kofman, W. (2021). Ultra-wideband SAR tomography on asteroids. *Radio Science*, *56*, e2020RS007186. https://doi.org/10.1029/2020RS007186

Received 12 AUG 2020
Accepted 22 JUL 2021

© 2021. American Geophysical Union. All Rights Reserved.

Ultra-Wideband SAR Tomography on Asteroids

Oriane Gassot[1], Alain Herique[1], Wenzhe Fa[2,3], Jun Du[2], and Wlodek Kofman[1,4]

[1]Univ. Grenoble Alpes, CNRS, CNES, IPAG, Grenoble, France, [2]School of Earth and Space Sciences, Institute of Remote Sensing and Geographical Information System, Peking University, Beijing, China, [3]State Key Laboratory of Lunar and Planetary Sciences, Macau University of Science and Technology, Macau, China, [4]Centrum Badan Kosmicznych Polskiej Akademii Nauk (CBK PAN), Warsaw, Poland

Abstract Our knowledge of the internal structure of asteroids is currently indirect and relies on inferences from remote sensing observations of surfaces. However, it is fundamental for understanding small bodies' history and for planetary defense missions. Radar observation of asteroids is the most mature technique available to characterize their inner structure, and Synthetic Aperture Radar Tomography (TomoSAR) allows 3D imaging of their interior. However, as the geometry of observation of small asteroids is complex, and TomoSAR studies have always been performed in the Earth observation geometry, its results in a small body geometry must be simulated to assess the methods' performances. We adopt here two different tomography algorithms and evaluate their performances in our geometry by assessing the resolution and the difference between the scatterer's position and its retrieved position. The first method, the Frequency Domain Back Projection (FDBP) is based on correcting the Fourier transform of the received signal by a phase function built from the geometry. While it can provide a good resolution, a bias remains in the imaged scatterer's position. Meanwhile, Compressive Sensing (CS) relies on the hypothesis that few scatterers lie in the same direction from the subsurface. Its application in the small body geometry is studied, which results in a slightly impoverished resolution but an improved localization of the scatterer.

1. Introduction

In standard high-resolution 2D Synthetic Aperture Radar (SAR) imaging, the spatial resolution along the slant-range direction is achieved by sending pulses with a wide bandwidth, and along the azimuth direction (along-track direction) by regularly sending pulses on a large synthetic aperture (Curlander & McDonough, 1991). However, because of the penetration of the waves, the returned echoes contain information about the surface under study as well as the subsurface and the resolution cell is spread in the third direction of space, perpendicular to the line-of-sight direction and the along-track direction. As the SAR image is a 2D mapping of the reflectivity of the scene, the resulting image is a projection of the reflectivities of the 3D volume to a 2D surface. Thus, image distortions may happen, such as layover, shadowing, or foreshortening, which degrade the 3D reconstruction of the scene and alter the imaged geometry. The third direction of space is named, hereafter, elevation, even if some authors use this name to refer to the range direction when projected on a 2D map.

Interferometric SAR (InSAR) (Ulander & Frolind, 1998) was first developed as an answer to this problem since it determines the height of a target by measuring the phase difference between several observations separated in space and/or in time. However, as the measured height is the height of the phase center of all the scatterers in the same range-azimuth cell, the position of each scatterer still cannot be resolved. Polarimetric SAR interferometry (Cloude & Papathanassiou, 1998) was then developed and was used to separate between surface and volume scattering effects within the same resolution cell and estimate their associated heights. However, this technique remains limited because it recovers only the mean height of all backscattering contributions in the same, large resolution cell. 3D SAR synthesis can also be considered, however, there is no resolution in the third dimension when imaging a surface with a single orbit.

SAR tomography was thus developed to overcome these limits. Its objective is to extend the synthetic aperture principle applied in the azimuth direction to the elevation direction, using 2D SAR images acquired with different positions in elevation. In this way, SAR tomography allows the reconstruction of a scene reflectivity profile along the elevation direction.

Since the first TomoSAR experiment (Reigber & Moreira, 2000), TomoSAR has received increasing attention and was applied to retrieve a forest's vertical structure (Cloude, 2007; Frey et al., 2008; Minh et al., 2016) or to reveal the inner structure of snowpacks (Frey et al., 2015), using its high-resolution capabilities. With the availability of SAR data with a high resolution, such as TerraSAR-X or COSMOS Skymes, high-resolution SAR tomography of urban areas began to be developed (Lombardini et al., 2009; Zhu & Bamler, 2010). Besides, in recent years, radar detections have been successfully performed to probe into planetary bodies' subsurfaces, such as the Moon (Nozette et al., 2010), Mars (Picardi et al., 2005; Seu et al., 2007), and on comets (Kofman et al., 2015). However, until now, all TomoSAR experiments have been conducted for large planetary surfaces but never applied to the smaller, kilometric bodies of our solar system.

The radar HFR, high-frequency radar, was developed in the frame of the Asteroid Impact And Deflection Assessment (AIDA)/Asteroid Impact mission (AIM) (Hérique et al., 2019b; Michel et al., 2016) to investigate the regolith of a kilometric asteroid with a submetric resolution, and TomoSAR algorithms are considered to improve the instrument's resolution in the elevation direction. However, as the geometry of observation of a small, kilometric body with HFR has several major differences with the Earth observation geometry (Section 2.2), the applicability of tomography algorithms is questioned.

This study presents the application of the Frequency Domain Back Projection (FDBP) and the Compressive Sensing (CS) TomoSAR algorithms on simulated SAR data obtained in an asteroid observation geometry. First, the characteristics of the observation of a small asteroid with HFR are presented, and the necessities of simulating the performances of TomoSAR algorithms in this geometry are highlighted. Then, different TomoSAR algorithms are described and the results of the FDBP are presented. Finally, the interests of CS for a small asteroid are presented, the method is implemented to improve the localization of an inclusion in the asteroid's subsurface, and its results are compared with those obtained by FDBP.

2. Radar Observation of Small Bodies From Orbit

The internal structure of asteroids remains largely unknown: without direct observation, our knowledge is mainly based on the analysis of optical remote observations of surfaces, inferences from gravitational field measurement, and physical modeling of evolution. Kilometric asteroids are expected to be rubbles piles: an aggregate of blocs gravitationally reaccreted after coalitional disruption, whose surface presents large blocks associated with regolith, mainly constituted of gravel and pebbles (Hérique et al., 2018 and included references). Ultra-wideband tomography is one of the key techniques to probe the first tens of meters of asteroid inner structure and to characterize the regolith, its structure, and the diversity of its constitutive material (Hérique et al., 2018). To better understand the stakes of the measurement, we present here the mission AIM (European Space Agency [ESA]), which boarded the HFR, designed for the specific observation of kilometric asteroids

2.1. AIM and HFR

In the frame of the mission AIDA , NASA's DART (Double Asteroid Redirection Test, Cheng et al., 2012), is a kinetic impactor designed to impact the moon of the binary asteroid (65803) Didymos, while ESA's AIM (Michel et al., 2016) was developed for its phase A/B1 to observe the asteroid structure state before and after the impact. The mission AIM was proposed to the ESA council 2016, but was unfortunately not funded to be launched in 2020 and reach Didymos in 2022.

Didymos is an S-type binary asteroid, consisting of a main body, which is about 800 m large, and its moon, which is about 160 m large. A preliminary shape model was derived using observations from Arecibo and Goldstone radars and photometric data.

Because of its small size, and thus mass, Didymos is supposed to have a weak gravity field. Its rotation period is slightly higher than 2.2 h, which is just above the limit of disruption for kilometric asteroids (Walsh & Richardson, 2008) and makes it a probable rubble pile. To fulfill its objectives, AIM boarded HFR to probe the asteroid's shallow subsurface, identify layerings, and link different surface measurements to the subsurface structure.

HFR (Hérique et al., 2018; Hérique, Plettemeier, Lange, et al., 2019) is a monostatic ultra-wideband, step frequency SAR, derived from the radar WISDOM (Ciarletti et al., 2017). This radar operates with frequencies ranging from 300 to 800 MHz in nominal mode and up to 3 GHz in an optional mode. HFR's frequencies are a trade-off between penetration depth, range resolution, and technical constraints, especially the antenna size (Hérique, Plettemeier, Kofman et al., 2019; Hérique, Plettemeier, Lange, et al., 2019). Indeed, a deep investigation requires low frequencies to reduce the dielectric and scattering losses, whereas subsurface probing requires a high resolution, achieved with a wide band, and thus high frequencies. HFR's band of 300–800 MHz allows probing the top 10 m of the asteroid subsurface with a resolution in the range direction better than 1 m, while the 3 GHz mode allows probing the surface with a higher horizontal resolution.

As an ultra-wideband radar studying a kilometric asteroid, HFR has major differences with classical radars, such as the ones used in the space-borne Earth observation. These differences are highlighted by considering HFR's scenarios of observation with AIM.

2.2. Scenarios of Observation

In a small body geometry, the motion of the radar with regard to a target on the asteroid is dominated by the rotation of the asteroid itself, while the spacecraft is considered motionless in an inertial frame: a point at the surface is then observed from its "rise" at the horizon until it is disappearing, with a relative velocity of less than 1 m per second.

To analyze the specificities of the small body observation, we consider a sequence of AIM observed as planned by ESA, computed using the NASA/SPICE library (https://naif.jpl.nasa.gov/naif/toolkit.html). The AIM spacecraft is motionless in an inertial frame at a distance of about 12 km from the asteroid's mass center. All computations and visualizations will be presented in a rotating frame linked and centered on the asteroid. After 30 min of observation, the spacecraft's trajectory is presented in this frame in Figure 1b, where the geometry's changes are dominated by the asteroid rotation.

This geometry of observation of Didymos with HFR has several major differences with the Earth observation geometry:

1. While in Earth observation, the radar's trajectory can be considered as rectilinear during the illumination time, in the observation of Didymos with HFR, the trajectory is dominated by the Didymos' rotation, as presented in Figure 1.
2. For Earth-observing radars, the surface observed can be considered planar in a first approximation due to the narrow antenna pattern. However, HFR's antenna beam covers the whole observed body, and the hypothesis of a plane surface for Didymos does not stand.
3. HFR is an ultra-wideband radar, with frequencies ranging from 300 to 800 MHz, which means that its band Δf is not negligible to its central frequency: $f_c : \frac{\Delta f}{f_c} = 0.91$, compared to classical spaceborne radars for which $\frac{\Delta f}{f_c} < 0.1$.
4. Earth-observing radars consider that the variation of slant range distance between the spacecraft and a given point of the scene is small during the observation. The same assumption can often be laid on the incidence angles when the observation time is sufficiently short. However, the geometry of the observation of Didymos is dominated by the body's rotation, and the whole asteroid is seen by HFR's antenna beam. Thus, the incidence angles and the slant-range distance cannot be easily approximated, and the range migration cannot be compensated.

Thus, classical hypotheses usually formulated for stripmap SAR in the Earth observation may not stand in the observation of small bodies, and the end-to-end performances of a given scenario can be evaluated from simulation only. Only in this way, any data-processing algorithms can be validated. Namely, since the range/Doppler separability cannot be assumed in this geometry, the SAR processing applied in our simulation is called "brute-force" and compensates the range and Doppler delays altogether.

With all of these differences, the classical point target pattern shaped as a product of two cardinal sines in the Earth observation geometry (Figure 2a) is not retrieved in the observation of Didymos and will depend

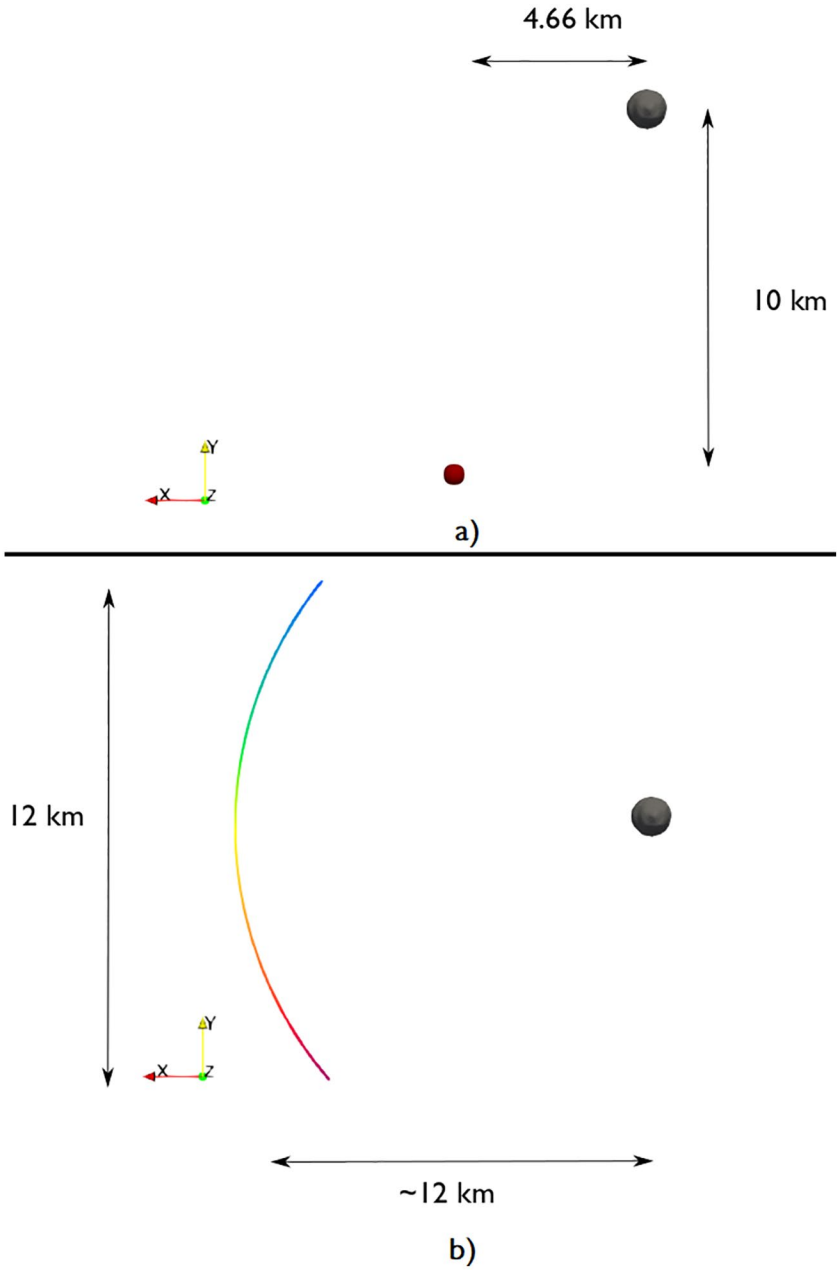

Figure 1. High-frequency radar (HFR)'s orbitography. The radar antenna (red) is motionless in an inertial frame (a), while the asteroid (gray) is moving. In a frame linked to the asteroid (b), the radar apparent motion is due to the asteroid rotation. Red depicts the beginning of the trajectory and blue the end.

on the scenario of observation and the radar's characteristics. In our simulations, the point target pattern acquires a “star-like” shape (Figure 2b).

HFR aims not only at studying the surface but the subsurface as well of small bodies, with a metric resolution in the third direction of space, the elevation direction. To compute this resolution, 3D SAR syntheses are necessary.

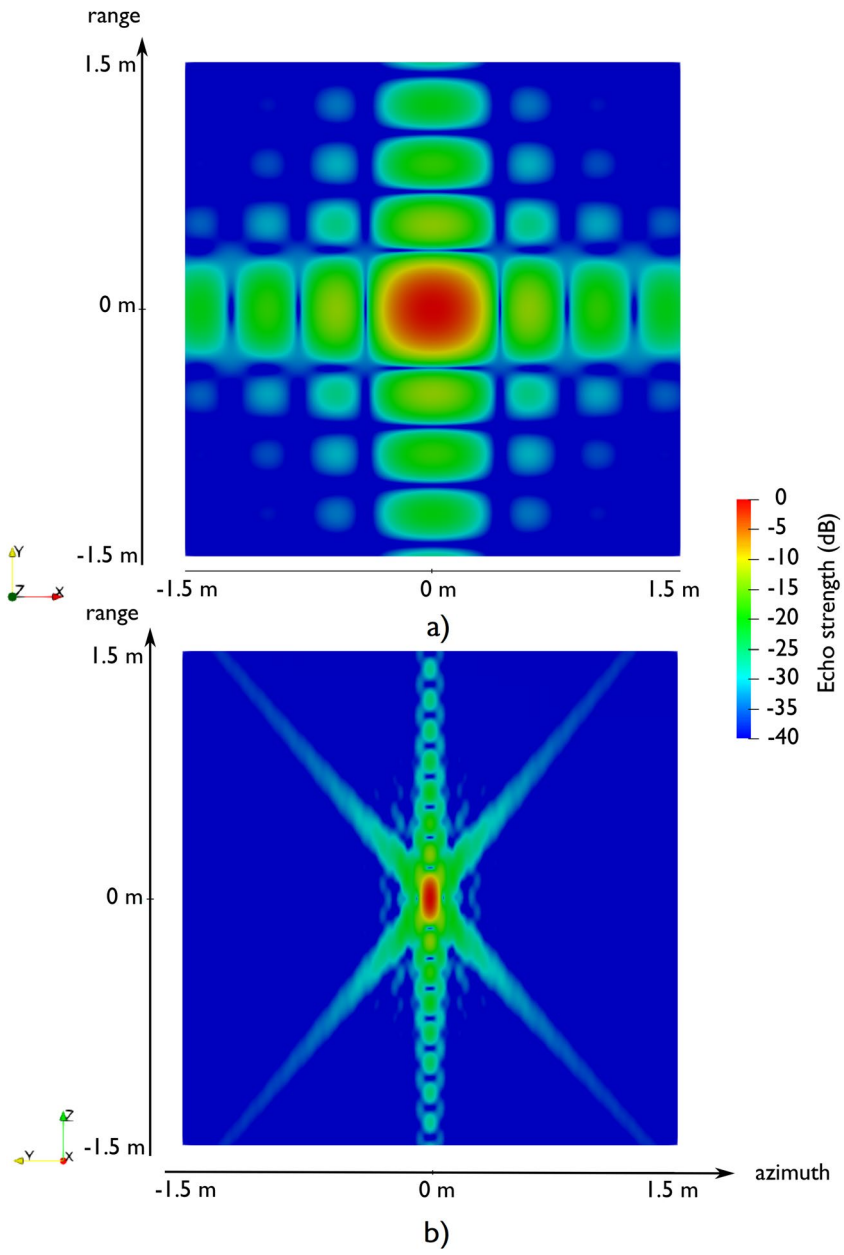

Figure 2. Examples of point target patterns. In the Earth observation geometry, the pattern is a product of cardinal sines in the range and the Doppler directions (a). The point target pattern in an asteroid observation geometry (b) depends on the geometry of observation and the radar characteristics and is shaped like a star in the observation of Didymos. The results are depicted with a 40-dB range dynamic normalized to the maximum power.

2.3. 3D SAR Synthesis

Using the scenario of observation described previously and computing the spectrum scattered by a point target, the 3D SAR synthesis of a target located at [0°, 0°] latitude and longitude on the surface of the asteroid was performed. The signal was simulated using the Simulation and Processing RAdar ToolS (SPRATS) toolbox, designed to simulate and interpret radar data in the frame of space mission analysis and preparation of spatial operations (Gassot et al., 2020). The synthesis is carried out using the FDBP algorithm, described by Soumekh (1999), which is based on the compensation of the phase of each scatterer during the observation.

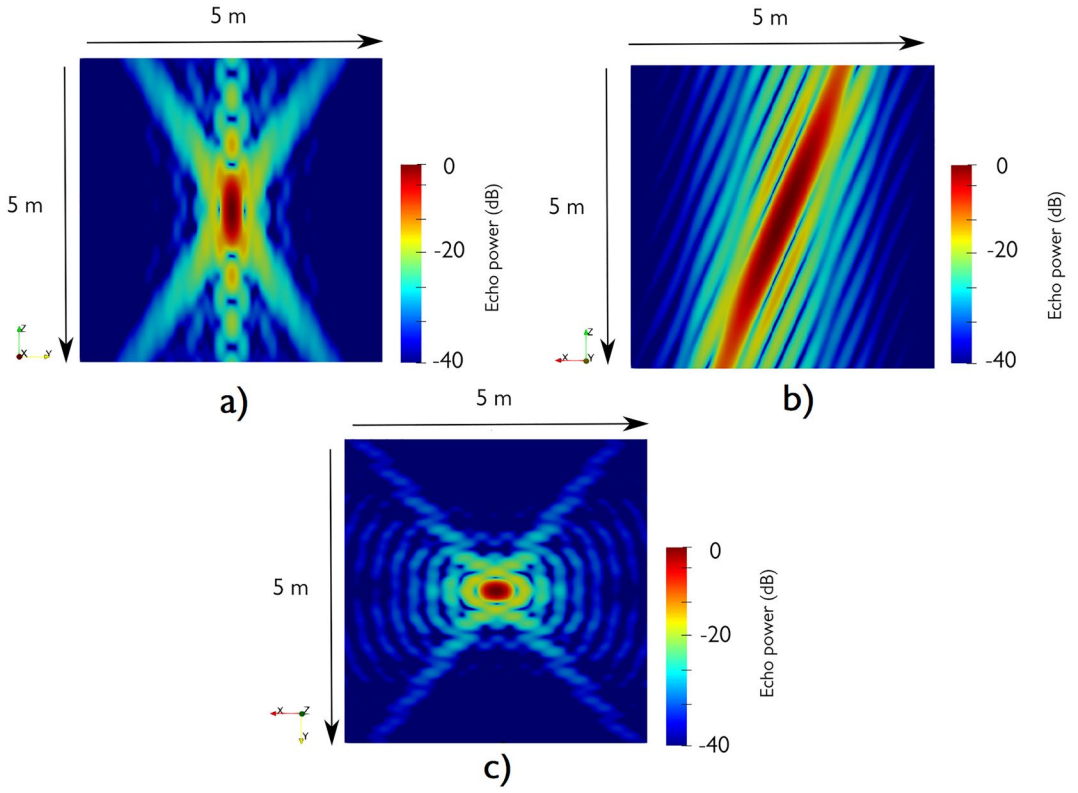

Figure 3. 3D Synthetic Aperture Radar (SAR) synthesis results along the *x*, *y*, and *z*-axis with a dynamic of 40 dB normalized to the maximum power. The elevation follows the [−0.4, 0.0, 0.93] direction.

The SAR synthesis is processed on a volume large of $5 \times 5 \times 5$ m^3 and is pictured in Figure 3. On the SAR image, high power is associated along the elevation direction (b), following roughly the [−0.4, 0.0, 0.93] direction. This feature is called elevation ambiguity. This ambiguity is an expected feature on spherical bodies when only one track is flown and illustrates that the target position in elevation is ambiguous. The elevation ambiguity is shaped like a straight tube in the Earth observation geometry but is shaped like an "hourglass" in the Didymos observation geometry. Indeed, as the trajectory is dominated by the asteroid rotation, it is not rectilinear and explores a few different elevation positions in the 3D domain. This allows focusing the target and explains why the target is imaged with a resolution in the elevation direction. As the trajectory is not aligned with the equatorial plane of Didymos, the ambiguity is defocused at all points in space, except at the position of the target. By measuring the width of the 3 dB spot presented in Figure 3, the resulting elevation resolution is computed to be 2.2 m with a single-track orbit, while the range resolution is 54 cm due to the 500 MHz bandwidth and the incidence of about 30°, and 21 cm in Doppler due to the 30 min observation duration. The elevation resolution is thus much poorer than the azimuth and range resolution and is not sufficient to probe the first tens meters of the subsurface.

HFR is a new instrument dedicated to the UWB study of asteroids, designed to probe an asteroid subsurface with a submetric resolution. However, any SAR observing a surface will have no resolution in the third direction with a single orbit. Since HFR's orbit is not rectilinear, the radar's trajectory will explore lightly the third direction (the elevation direction), and the resolution in the elevation direct exists but is too poor to comply with the objectives of HFR to probe an asteroid with a resolution of less than 1 m in the vertical direction. Tomography algorithms are a solution to improve the elevation resolution and probe the subsurface with a decimetric resolution.

3. SAR Tomography

TomoSAR algorithms have been developed to recover the 3D structure of embedded objects or reconstruct anthropic structures in urban areas. They can be classified into three main families:

3.1. Traditional 2D SAR Imaging Algorithms Applied in the 3D Domain

They can be organized into frequency and time domain algorithms:

1. The frequency-domain methods, such as the SPECAN (SPECtral ANalysis, Reigber & Moreira, 2000), operate a Fourier transform to focus the received signal along the elevation direction. Their main appeal is their low computational burden. However, it is challenging to observe a scene with evenly distributed flight tracks: the received data are always undersampled due to the small number of observations, and an additional interpolation procedure is always needed, which increases the computational burden and reduces the interest of these methods.
2. The time-domain methods, such as the TDBP (Time-Domain Back Projection) method (Nannini & Scheiber, 2006) directly focus the signal in elevation with an ad hoc function. These methods do not rely on the regular distribution of flight tracks, but are time-consuming. The TDBP can be expressed in the frequency-domain and is then called FDBP (Frequency Domain Back Projection, Soumekh, 1999).

3.2. The Polarimetry Coherence Tomography (PCT)

This method uses POLInSAR data to derive the elevation reflectivity function, characterized by the Fourier Legendre series. Using a single or dual baseline architecture, the PCT method has been implemented to derive the elevation profile of the radar scattering intensity, while avoiding any flight track control (Cloude, 2006). However, PCT relies on a priori knowledge on the height of the scattering volume and the phase of the ground, which adds some additional procedures when this knowledge is lacking and increases its computational load. Finally, with a small number of baselines, the spatial resolution of the PCT tomogram is poorer than different tomography methods.

3.3. The Spectral Estimation (SE) Methods

These methods are high-resolution TomoSAR algorithms, which are based on an inversion problem between the measurement vector and a matrix called the mapping matrix to retrieve the vector reflectivity profile. Two families exist:

1. Parametric models, such as the MUSIC (MUltiple SIgnal Classification) algorithm (Nannini et al., 2011) are easily implemented but require a priori information on the surface to be imaged, such as the number of scatterers.
2. Nonparametric models, such as the CS (Compressive Sensing) algorithm (Zhu & Bamler, 2010) are more flexibles but rely on hypotheses on the investigated geometry that may be hard to satisfy.

Ultimately, the choice of one method instead of another relies on the characteristics and requirements of the study, since each of these models has its advantages and drawbacks. From their description, we summarize the strengths and weaknesses of each model in Table 1, which classifies the different methods depending on their computational burden, their resulting spatial resolution, the operation complexity (the difficulty to carry on the observation in a nominal way), and the adaptability of the algorithm to correct the delay induced by the permittivity of the subsurface.

In this study, we focused on methods based on SAR processing: backpropagation methods associated with a modeling of the SAR response. There are of course additional families of tomography methods, in particular, inversion by forward modeling and iterative minimization of the distance between the measurement and the forward simulations (Sava & Asphaug, 2018a, 2018b and in a bistatic configuration with Pursiainen & Kaasalainen, 2016 or Eyraud et al., 2018). In parallel to the presented work, such tomography methods are being evaluated in the framework of the HERA/Radar JuRa scientific group. It should be noted that backpropagation methods present significant interest at least as a first processing run, especially to analyze

Table 1
TomoSAR Algorithms Performances as Analyzed in Referenced Papers

	Computational burden	Spatial resolution	Complexity	Adaptability to a change of ε	Reference
SPECAN	Medium	Medium	High	Low	Reigber and Moreira (2000)
FDBP	High	Medium	Medium	Low	Nannini and Scheiber (2006)
PCT	Low	Low	Low	Medium	Cloude (2006)
CS	Medium	High	Medium	Medium	Zhu and Bamler (2010)

Abbreviations: CS, compressive sensing; FDBP, frequency domain back projection; PCT, polarimetry coherence tomography; SPECAN, SPECtral ANalysis; TomoSAR, synthetic aperture radar tomography.

the robustness due to a lack of data, and to easily implement autofocus algorithms to estimate and compensate orbitography errors.

Given the high resolution provided by the radar, the range migration caused by the different orbits will exceed half the resolution cell size in our scenario, which excludes frequency domain methods as well as spectral estimation methods for a correct reconstruction of the reflectivity profile. Since we applied the FDBP to compute the 2D SAR synthesis, its 3D-domain application is a natural first choice to be applied in tomography.

3.4. Scenario of Simulation

3.4.1. Orbitography

To validate the method and evaluate the performances, we first simulate a data set for a scenario of observation. We consider the signal backscattered by an inclusion embedded in the asteroid subsurface for several elevation incidences, which are described by the spacecraft's orbitography.

Our scenario of observation considers the orbit described in Section 2.2, repeated 20 times, with an offset of 500 m between each track. The resulting geometry of observation is presented in Figure 4.

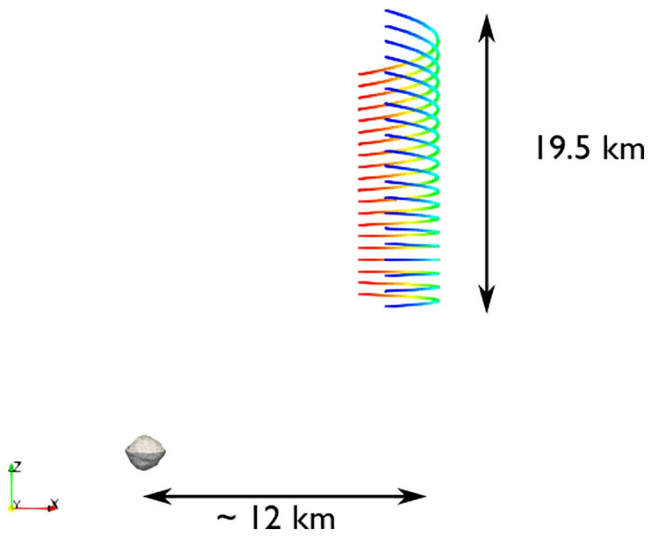

Figure 4. The trajectories used for the Synthetic Aperture Radar Tomography (TomoSAR) algorithms. This view is in a Didymos centered frame. The red part pictures the beginning of the trajectory and the blue the end.

3.4.2. Asteroid's Regolith Model

Setting up a dielectric model of an asteroid is definitively challenging for both the regolith and the inert structure. While the dielectric permittivity of the constitutive material is well constrained from direct measurement and dielectric mixture modeling (see review in Hérique et al., 2016), little information is available on the structure given the lack of direct measurements. The crucial question is the macro-porosity: are large voids present between larges blocks or are pebbles and material filling in the voids between the blocks. For Bennu's interior, recent analyses indicate a limited macroporosity (Grott et al., 2020) and thus points to the second solution. For the regolith, the surfaces show the presence of fine material and no large macroporosity, which corresponds to a formation by thermal and mechanical fragmentation. In this study, we will consider a mostly homogeneous regolith consisting of sand and gravels, modeled as a medium with a permittivity of 3.0, filled with several larger rock inclusions. We consider for now that few rock inclusions lie in the same elevation profile.

We consider an inclusion located at 25 cm under the asteroid surface. The surface is modeled as a $50 \times 50\text{-cm}^2$ large mesh of 20×20-point facets with a constant permittivity of 3.0, the permittivity of dry sand, which is similar to the texture expected from rocky asteroids surfaces (Hérique, Plettemeier, Kofman et al., 2019). The inclusion is modeled with a permittivity of 3.1, embedded in a subsurface, associated with a permittivity of 3.0.

Table 2
Simulation Parameters

Simulation parameters	
Radar central frequency	550 MHz
Radar bandwidth	500 MHz
PRF	0.12 Hz
Surface size	50 cm
Surface Sampling	2 cm
Inclusion size	1.5 cm
Volume permittivity	3.0
Inclusion permittivity	3.1

3.4.3. Simulation of the Signal

The spectrum scattered by the surface is computed using the facet method, which estimates the field scattered by each facet by applying the Fresnel coefficients and computes the facet's scattering lobe. The facet method was implemented using SurfaceEchoPO (Berquin et al., 2015; Nouvel et al., 2005).

The field transmitted by the surface to the inclusion is computed with the facet method as well, while the field backscattered by each inclusion is computed using the Born Approximation (Ulaby et al., 1986). The method considers that the field inside a volume of average permittivity ε_a, perturbed by different inclusions of permittivity ε_f, is equal to the field that would be present without the inclusions. Then, the field scattered by each inclusion can be computed from the field inside the volume. This approximation is valid only if the contrast in the dielectric permittivity between the inclusion and subsurface $\Delta\varepsilon$ is small. In our scenario, $\varepsilon_a = 3.0$ and $\Delta\varepsilon = 0.1$. The parameters of the simulation are summarized in Table 2.

Before presenting the TomoSAR results of the scenario, one should note that the simulations of the scattered spectrum do not cover any process gain, antenna gain, or synthesis gain. Moreover, they do not consider any gain that may be reached with the range/Doppler compression. By additionally considering the very small size of the volume under study, in the end, the power of the scattered spectrum will be very low. However, the goal of this study is to validate the reconstruction of an inclusion with TomoSAR, and not to estimate its behavior in a physical, realistic scenario. This would be performed in further studies once the behavior of the TomoSAR in a small body geometry is validated.

3.5. Application of the TomoSAR FDBP

3.5.1. Description of the TomoSAR FDBP

The FDBP is presented in 2D imaging in Soumekh (1999) and achieves focusing by using the geometry between the sensor and the imaged volume: every resolution cell of the 3D SAR image is focused based on the true acquisition geometry and a reference function. The TomoSAR FDBP is based on the same principle and considers 3D SAR images $s_n\left(\vec{r}_i\right)$, already focused on the range/doppler plan. For each track, the image s_n corresponds to the nth flight track:

$$s_n\left(\vec{r}_i\right) = \sum_{j=a_n}^{b_n} S\left(f_m\right) \cdot \exp\left(i4\pi f_m \frac{R_{nij}}{c}\right) \tag{1}$$

with S: the measured spectrum; $\vec{r}_i$: the position of the scatterer; a_n, b_n: the indexes of the first and last azimuth position of the sensor; $\overrightarrow{r_{S\,jn}}$: the position vector of the sensor of the nth track; $R_{nij} = \left|\vec{r}_i - \overrightarrow{r_{S\,jn}}\right|$: the range distance, considering the waves follow straight paths; f_m : the frequency.

The TomoSAR image v is then the sum of all spectra for all tracks and can be written at the position $\vec{r}_i$:

$$v\left(\vec{r}_i\right) = \sum_{n=1}^{N} \sum_{j=a_n}^{b_n} S\left(f_m\right) \cdot \exp\left(i4\pi f_m \frac{R_{nij}}{c}\right) \tag{2}$$

As a TomoSAR algorithm, the resolution expected from FDBP can be obtained by (Reigber & Moreira, 2000):

$$\delta_e = \frac{\lambda r_0}{2L} \tag{3}$$

where λ is the wavelength, r_0 is the range distance, and L the distance covered by all trajectories in the elevation direction. Considering that $L = 8.33$ km in our scenario, the expected resolution was computed to be 39 cm.

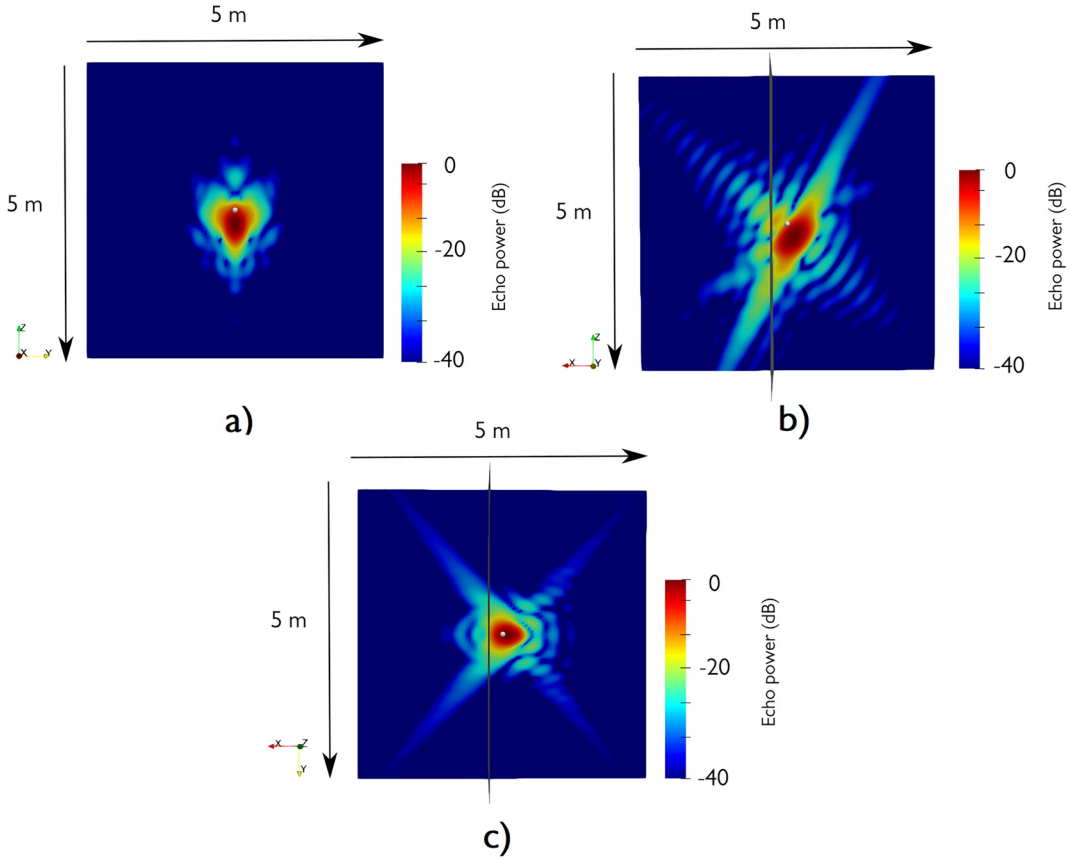

Figure 5. Frequency Domain Back Projection (FDBP) Synthetic Aperture Radar Tomography (TomoSAR) results along the *x*, *y*, and *z*-axis, with a dynamic of 40 dB normalized to the maximum power. The gray sphere pictures the theoretical position of the target, and the surface is represented to help visualize the geometry.

3.5.2. Numerical Results

The FDBP was applied to our scenario and its result is presented in Figure 5, with the position of the target highlighted by a gray sphere. The elevation resolution achieved with the multipass geometry is improved from 2.2 m and reaches 47 cm, which is comparable to the 39 cm theoretical resolution expected from TomoSAR algorithms. The theoretical resolution is not reached because its expression was carried out in the Earth observation geometry and not in our specific small body geometry. However, the position of the target cannot be retrieved by the FDBP. Indeed, the SAR processor does not know the medium permittivity, and the position of the target is then shifted.

Traditionally, ray tracing methods are implemented to correct the delay induced by the propagation of the wave in a medium where the permittivity is different from 1.0. These methods can be used for tomography of a small body (Kofman et al., 2015), but in UWB their stability relies on a precise shape model, and will not be considered. We note here that TomoSAR algorithms make similar hypotheses to the ray tracing: straight propagation of the waves and constant velocity. However, while the FDBP considers that the waves always propagate in the void, CS is an additional TomoSAR algorithm that considers the straight path of the waves in the void at the velocity of light, and a different straight path in the subsurface at a lower velocity. Hence, CS uses the same hypotheses as ray tracing in the two different media but computes the crossing of the interface to link them, which allows retrieving the structure of the subsurface directly from the SAR images.

3.6. Reconstructing the True Position of the Target With the Compressive Sensing

To reconstruct the true position of the target, additional tomography methods can be considered. CS is a spectral estimation method based on the computation of SAR images on the surface of the volume

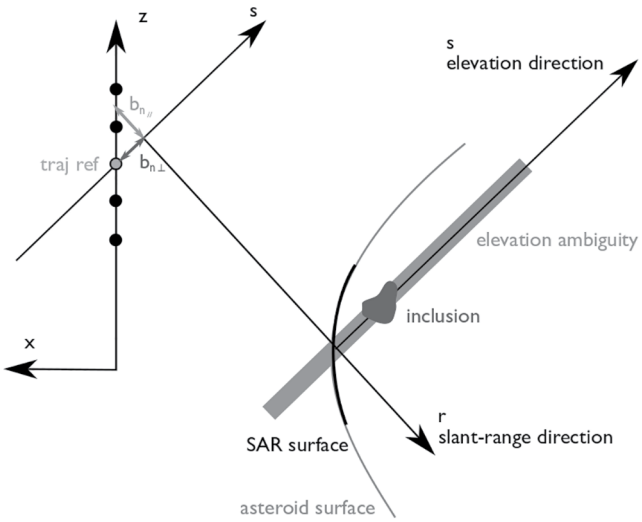

Figure 6. Compressive Sensing geometry in a small body geometry. The different tracks are represented as black spots in the *z*-direction, and the reference track is highlighted.

investigated, and on the retrieval of the reflectivity profile in the elevation direction, if this reflectivity profile is sparse. This means that the CS treats the propagation of the waves in the void (by computing the SAR image at the surface) and the subsurface (by computing the reflectivity profile of the subsurface) separately. Thus, the compensation of the delay can be carried out more easily than by correcting the SAR processing. However, the CS is not entirely adapted in a geometry where the range migration exceeds the size of the resolution cell, which is the case in our small body geometry. As a consequence, the performances of the CS will deviate from the nominal performances and will not be as high as the performances achieved with the FDBP. Nevertheless, by treating the propagation of the wave in two steps, in the void and the subsurface, the CS can be applied to retrieve the true position of the scatterers. Additionally, in the case, the elevation profile is not sparse, it may not be entirely resolved by the CS.

3.6.1. TomoSAR Using Compressive Sensing

In a multipass SAR acquisition, the value of a SAR pixel *g* located at the position (*x*, *r*) corresponds to the integral of the reflected signal along the elevation direction:

$$g_n(\mathrm{x},\mathrm{r}) = \int_s \gamma(x,r,s)\exp\left(-\frac{4j\pi}{\lambda}d_n(x,r,s)\right)ds \tag{4}$$

with *n* indicating the position of the pass in a multipass geometry, *s* is the elevation position, γ is the pixel's reflectivity, d_n is the distance from the radar to each pixel, and λ is the wavelength. Following the derivation developed by Fornaro et al. (2003), which was carried out in the Earth observation geometry, by defining a reference track, we find that:

$$g_n(\mathrm{x},\mathrm{r}) = \int_s \gamma(s)\exp\left(2j\pi\frac{2}{\lambda}\frac{b_{n\perp}}{(r-b_{n\parallel})}\right)ds \tag{5}$$

where $\gamma(x,r,s)$ is written $\gamma(s)$ for simplicity, *r* is the slant range distance between the surface and the reference track and $b_{n\perp}$ and $b_{n\parallel}$ are the parallel and orthogonal distances between each track and the reference track, as presented in Figure 6.

Thus, by discretizing the continuous elevation function *s*, we can write:

$$\boldsymbol{g} = R\boldsymbol{\gamma} \tag{6}$$

where *g* is the measurement vector, γ is the elevation reflectivity profile vector, and *R* is a matrix called the mapping matrix, expressed as:

$$R_{nl} = \exp\left(-2j\pi\cdot\frac{f_n}{c}\cdot s_l\right) \tag{7}$$

with:

$$f_n = -2f\cdot\frac{b_{n\perp}}{(r-b_{n\parallel})} \tag{8}$$

where s_l depicts the discretization of the elevation vector and f is the central frequency of the signal. The matrix R_{nl} was computed considering that the waves follow straight paths.

The objective of TomoSAR is to retrieve the elevation profile $\gamma(s)$ for each azimuth-range pixel (*x*, *r*), which is performed by an L_1-norm minimization:

$$\hat{\boldsymbol{\gamma}} = argmin\{\|\boldsymbol{\gamma}\|_1\}\, s.t\, \boldsymbol{g} = R\boldsymbol{\gamma} \tag{9}$$

This minimization can be easily achieved with basis pursuit methods (Van den Berg & Friedlander, 2011).

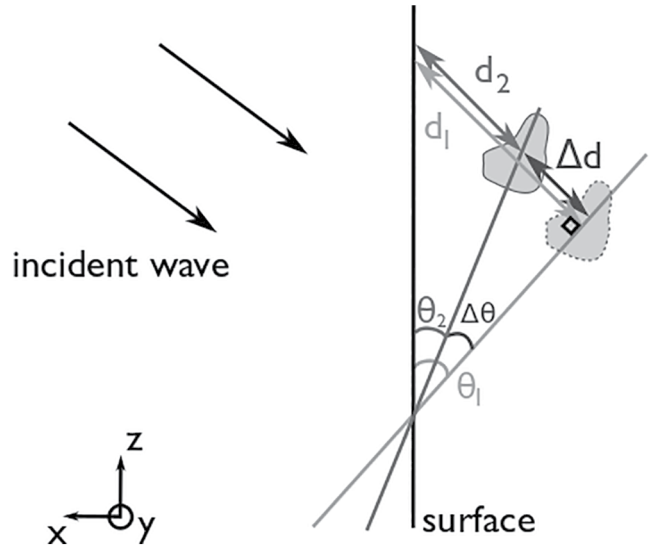

Figure 7. Illustration of the measurement error induced by the permittivity of the medium.

3.6.2. Correction of the Delay

One of the main attractions of CS is its potential to correct the delay induced by the propagation of the wave in the subsurface. The compensation of the delay of the signal can be understood by considering a target embedded under a surface. Because the SAR processor considers that the signal is always propagating in the void, the final SAR image sees any point below the surface located deeper than it is. This means that the elevation ambiguity in the void and the subsurface will not have the same orientation, yet the SAR processor will consider the elevation ambiguity has always the orientation of the voids. Thus, as illustrated in Figure 7, targets lying at an angle θ_2 from the point on the surface with the same range/azimuth delay, will be imaged at an angle θ_1.

As the CS aims at retrieving all scatterers in the elevation direction, the compensation of the delay can be carried out by first retrieving all scatterers on the elevation profile, computed in the void. Then, considering that the wave's velocity is roughly constant in this relatively homogeneous medium and performing a rotation by an angle $\Delta\theta$ and dilatation of parameter $\frac{1}{\cos(\Delta\theta)}$, we retrieve the actual elevation profile in the medium, with:

$$\Delta\theta = \theta_2 - \theta_1 = atan\left(\left(1 - \frac{1}{\sqrt{\varepsilon_a}}\right) \cdot \tan(\theta_1)\right) \tag{10}$$

3.6.3. Numerical Results

20 2D SAR images of the scenario described in Section 3.1 were computed at the surface of the asteroid, and the CS method was then implemented with a basis pursuit method algorithm, using the SPGL1 algorithm with the SPGL1 python library (Van den Berg & Friedlander, 2008). For each pixel of the SAR image, the reflectivity profile γ was retrieved on an elevation profile 3 m in length, with a sampling of 3 cm. First, the CS results without the compensation of the delay are presented in Figures 8a–8c, with a dynamic range of 40 dB. The theoretical position of the target is indicated with a gray sphere.

Figure 8 highlights that CS retrieves the signal by maximizing its sparsity. Thus, when a profile does not largely contribute to the signal, CS sets the entire profile to 0, which explains the abrupt variation of the retrieved reflectivity. The difference between the position of the located target and its theoretical position is due to the delay produced by the permittivity of 3.0 and is expected since no compensation of the delay was performed. No sidelobes appear in the range or doppler dimensions since they are taken into account in the reflectivity model. The CS achieves an elevation resolution of 60 cm, which is worse than the 47 cm resolution achieved with the FDBP, as presented in Table 3. This difference is expected since the conditions of the application of the CS are not fully retrieved in our geometry.

CS was then applied with the correction of the delay, and the results are presented in Figures 8d–8f. As expected, the compensation of the delay improves the localization of the target, which falls into the 3-dB width spot, with a resolution of 61 cm. The comparison of the resolution achieved with the different methods is presented in Table 3. Further differences between the localization of the target and its true position may be due to additional refraction effects.

As the CS is performed, starting from a stack of SAR images using the Born Approximation, the results obtained with CS are linked to the Born Approximation's limits. Indeed, the asteroid's surface is described as a mesh of facets. To keep the far-field hypothesis correct for all inclusions in the sub-surface, the facets must be designed small enough to behave a point targets, which requires a large sampling and thus causes long computation times. Further improvement will have to be carried out on the Born Approximation to reduce the computation time, to test the CS with scenarios with a larger number of inclusions or larger volumes, which could be used to further validate the model.

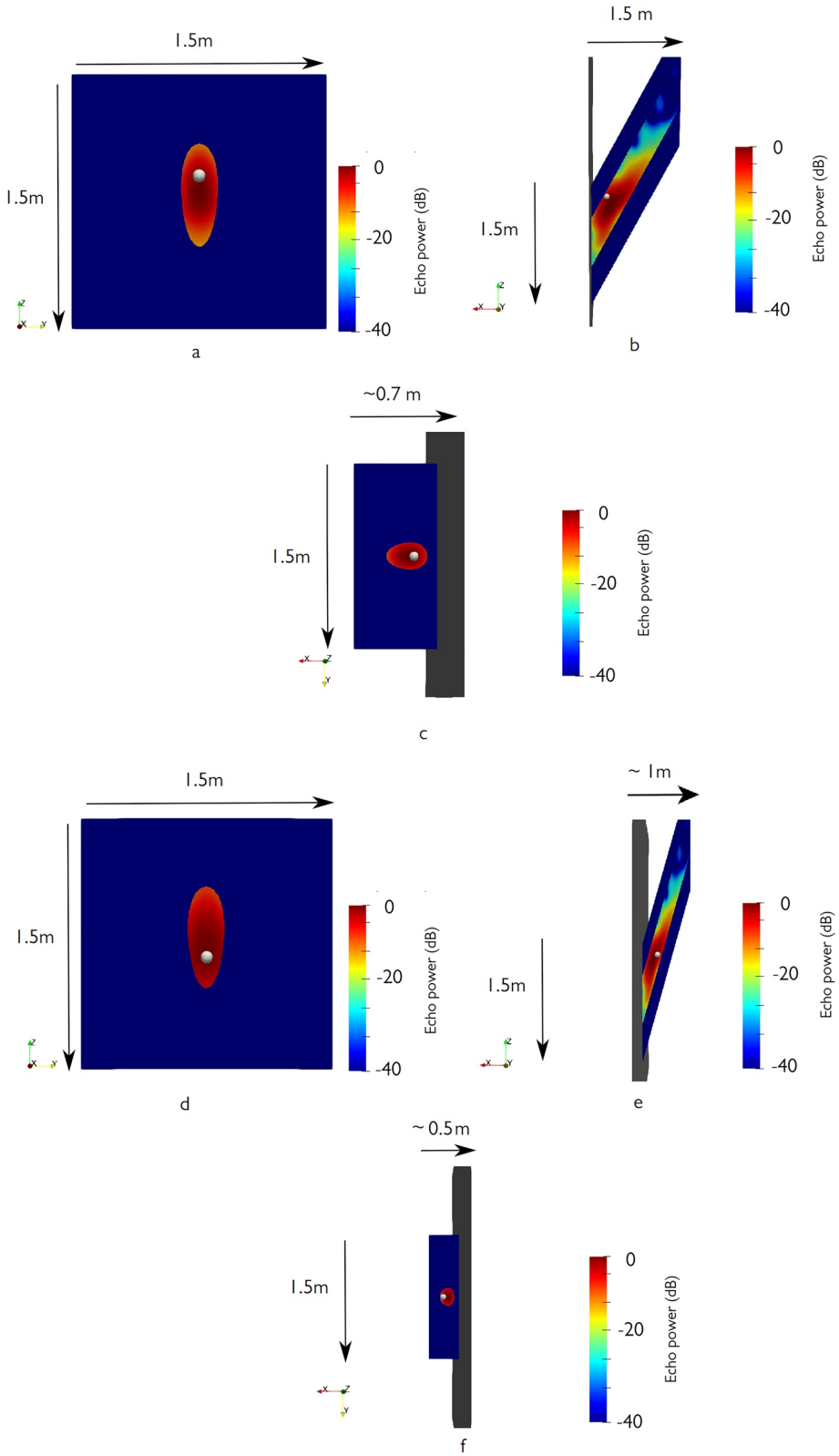

Figure 8. (a–c) Compressive Sensing results along the *x*, *y*, and *z* axis, with a dynamic of 40 dB normalized to the maximum power. (d–f) Compressive Sensing results along the *x*, *y*, and *z* axis, with a dynamic of 40 dB normalized to the maximum power by compensating the phase delay, considering that the target is located in a medium with a permittivity of 3.0. The gray sphere indicates the theoretical target position.

Table 3
Comparison of the Resolution Achieved With the Different Imaging Methods

	Single pass	Theoretical (TomoSAR)	Multipass synthesis	CS
Resolution (m)	2.2	0.39	0.47	0.6

4. Conclusions

The UWB radar HFR was developed to observe the first 10 m of asteroids' subsurface, with a sub-metric resolution. To improve the resolution in elevation, tomography methods can be carried out. We present in this paper how the Frequency-Domain Back-Projection method (FDBP) TomoSAR is implemented in a small body geometry and images a single embedded inclusion with a resolution of 47 cm. However, the method cannot reconstruct the position of the inclusion when the permittivity of the subsurface is different than one, and the ray-tracing methods which could be applied to correct the position are unreliable in UWB small body geometry. Yet, by modeling the asteroid subsurface as few point-like scatterers, the reflectivity profile of each point of the asteroid surface is sparse, and the CS can be applied. The CS method consists of an L1-norm minimization and was applied to the reconstruction of scatterers in urban areas (Zhu & Bamler, 2010). Yet, it was never applied in an asteroid geometry and the fact that range migration is higher than the resolution cell size invalidates its application. Nevertheless, the CS allows improving the localization of the target with the knowledge of the medium permittivity. We presented in this study how the CS was applied in the small body geometry. The resolution retrieved by the CS is worse than the resolution retrieved by the FDBP, which is expected since the hypotheses of the application of the CS are not retrieved, but the CS manages to retrieve the position of the scatterer.

The CS cannot yet be tested with several targets because of computational limitations with our current volume scattering model, the Born Approximation. Different works are under study to overcome these limitations and would be needed to test the performances of CS to distinguish between closely separated scatterers.

Even though the mission AIM was not funded in 2016, the mission Hera (Michel et al., 2018) is an updated version of AIM. On Hera, the small Juventas will board JuRa, Juventas Radar, a low-frequency monostatic radar with frequencies ranging from 50 to 70 MHz to study the inner structure of Didymos (Hérique, Plettemeier, Kofman et al., 2019). Hera and JuRa will benefit from the results of the applicability and the performances of the CS on the Didymos geometry, since the observation geometry stays the same, despite the change of frequencies, and thus, of resolution.

Further work on the CS application will focus on overcoming the Born Approximation limitations, and simulate the behavior of several pointlike targets, as well as several larger targets and test the CS performances.

Appendix A: Compressive Sampling

Compressive sampling is a technique adapted to the reconstruction of sparse signals (Candès & Wakin, 2008). A signal x of length L is said K-sparse in an orthogonal basis ψ if the projection of x onto ψ, $\boldsymbol{s} = \psi \boldsymbol{x}$ has only K nonzero elements.

If a measurement vector of size N s is obtained by projecting $\boldsymbol{x}$ onto a matrix Φ, where Φ is called the sensing matrix, then we can write:

$$\mathbf{y} = \Phi\, \boldsymbol{x} = \Phi\, \psi^H \boldsymbol{s} = \Theta \boldsymbol{s} \tag{A1}$$

where Θ is called the mapping matrix, and H stands for the conjugate transpose operator.

Using the compressive sampling method, s can be reconstructed by L_0-norm minimization, which finds the solution of Equation 1 with the minimum number of non-zero coefficients:

$$\hat{\boldsymbol{s}} = argmin\left\{\| \boldsymbol{s} \|_0\right\} s.t\ \boldsymbol{y} = \Theta \boldsymbol{s} \tag{A2}$$

For sparse signals, the L_0-norm minimization and the L_1-norm minimization leads to the same results. Thus, s can be found using the L_1-norm minimization:

$$\hat{\boldsymbol{s}} = argmin\left\{\| \boldsymbol{s} \|_1\right\} s.t\ \boldsymbol{y} = \Theta \boldsymbol{s} \tag{A3}$$

This minimization can be performed using basis pursuit methods (Van den Berg & Friedlander, 2008). To have a unique solution:

1. The sensing matrix Φ and the orthogonal basis ψ must be incoherent, in order not to bias the reconstruction of non-zero elements into certain positions. The incoherence can be computed as:

$$\mu(\Phi,\psi) = \sqrt{n} \cdot \max\left|\left\langle \Phi_k \psi_j \right\rangle\right| \quad 1 < k, j < n \tag{A4}$$

where n depicts the number of columns of Φ and ψ, k and j depicts the index of the col

1. The mapping matrix Θ must follow the Restricted Isometry Property (RIP), which guarantees a sufficiently sparse reconstruction in the presence of noise:

$$\left(1-\delta_s\right) \| \boldsymbol{v} \|_2^2 \leq \| \Theta \boldsymbol{v} \|_2^2 \leq \left(1+\delta_s\right) \| \boldsymbol{v} \|_2^2$$

where $\boldsymbol{v}$ is any K-sparse vector, with non-zero coefficients at the same position as s, and δ_s is a small number. The smaller δ_s the better the sparse signal will be reconstructed in the presence of noise. This property assures that Θ preserves approximately the Euclidean length of the sparse signals. This implies that these vectors cannot be in the null space of Θ and can thus always be recovered and that all distances between sparse signals will be reconstructed in the measurement space.

Appendix B: TomoSAR Using CS

The Compressive Sensing method applied to TomoSAR imagery seeks to solve:

$$\hat{\boldsymbol{\gamma}} = argmin\left\{\| \boldsymbol{\gamma} \|_1\right\} s.t\, \boldsymbol{g} = R\boldsymbol{\gamma} \tag{A5}$$

where γ the reflectivity profile, g is the SAR image pixel, and R and a matrix composed of factors computed from the distance between the spacecraft and the surface.

Given that:

1. The signal γ is sparse since we consider only a few inclusions lie in each elevation direction of each SAR pixel.
2. The orthogonal basis matrix ψ is the identity matrix in our geometry. As the distance between the radar to each SAR pixel is large considering the wavelength, the R matrix can be considered random. R and ψ are thus incoherent.
3. The RIP property is verified: In the case of a single scatterer, the RIP property is automatically verified. When imaging several scatterers, the RIP is verified if the scatterers are separated by a distance larger than the resolution (Zhu & Bamler, 2010).

As these hypotheses are validated, the CS can be applied to our study.

Data Availability Statement

The code described in this study is described in Kong (1990) for the facet method, Soumekh (1999) for the FDBP and Zhu and Bamler (2010) for the CS. The scripts and resulting data used for supporting the figure results can be found in: Gassot et al., 2020, Ultra-wideband SAR Tomography on asteroids: FDBP and Compressive Sensing datasets, Version 1. August 2020, Univ. Grenoble Alpes, CNRS, CNES, IPAG, 38000 Grenoble, France. https://doi.org/10.5281/zenodo.3981252. Accessed 2020-08-12.

Acknowledgments
Hera is the ESA contribution to the AIDA collaboration. Juventas and JuRa are developed under ESA contract supported by national agencies. JuRa is built by Emtronix (Lux), UGA/IPAG (Fr), TUD (Gr), Astronika (Pl), and BUT (Cz). Juventas is built by Gomspace (Lux). This work has been supported by ESA's General Studies Program (AIM Phase A and UWBTO study).

References

Berquin, Y., Herique, A., Kofman, W., & Eggy, E. (2015). Computing low-frequency radar surface echoes for planetary radar using Huygens-Fresnel's principle. *Radio Science*, *50*(10), 1097–1109. https://doi.org/10.1002/2015rs005714

Candès, E. J., & Wakin, M. B. (2008). An introduction to compressive sampling. *IEEE Signal Processing Magazine*, *25*(2), 21–30. https://doi.org/10.1109/msp.2007.914731

Cheng, A. F., Michel, P., Reed, C., Galvez, A., & Carnelli, I. (2012). Dart: Double asteroid redirection test. *European Planetary Science Congress*, *7*, 23–28.

Ciarletti, V., Clifford, S., Plettemeier, D., Gall, A. L., Hervé, Y., Dorizon, S., et al. (2017). The WISDOM radar: Unveiling the subsurface beneath the ExoMars Rover and identifying the best locations for drilling. *Astrobiology*, *17*(6–7), 565–584. https://doi.org/10.1089/ast.2016.1532

Cloude, S. R. (2006). Polarization coherence tomography. *Radio Science*, *41*(4). https://doi.org/10.1029/2005rs003436

Cloude, S. R. (2007). Dual-baseline coherence tomography. *IEEE Geoscience and Remote Sensing Letters*, *4*(1), 127–131. https://doi.org/10.1109/lgrs.2006.885893

Cloude, S. R., & Papathanassiou, K. P. (1998). Polarimetric SAR interferometry. *IEEE Transactions on Geoscience and Remote Sensing*, *36*(5), 1551–1565. https://doi.org/10.1109/36.718859

Curlander, J. C., & McDonough, R. N. (1991). *Synthetic aperture radar: Systems and signal processing* (p. 170). Wiley series in remote sensing.

Eyraud, C., Herique, A., Geffrin, J. M., & Kofman, W. (2018). Imaging the interior of a comet from bistatic microwave measurements: Case of a scale comet model. *Advances in Space Research*, *62*(8), 1977–1986. https://doi.org/10.1016/j.asr.2017.10.012

Fornaro, G., Serafino, F., & Soldovieri, F. (2003). Three-dimensional focusing with multipass SAR data. *IEEE Transactions on Geoscience and Remote Sensing*, *41*(3), 507–517. https://doi.org/10.1109/tgrs.2003.809934

Frey, O., Morsdorf, F., & Meier, E. (2008). Tomographic imaging of a forested area by airborne multi-baseline P-band SAR. *Sensors*, *8*(9), 5884–5896. https://doi.org/10.3390/s8095884

Frey, O., Werner, C. L., & Wiesmann, A. (2015). Tomographic profiling of the structure of a snowpack at X-/Ku-Band using SnowScat in SAR mode. In *2015 European radar conference (EuRAD)* (pp. 21–24). IEEE. https://doi.org/10.1109/eurad.2015.7346227

Gassot, O., Hérique, A., Rogez, Y., Kofman, W., Zine, S., & Ludimbulu, P. P. (2020). SPRATS: A versatile Simulation and Processing RAdar ToolS for planetary missions. *IEEE radar conference (RadarConf20)* (pp. 1–5). https://doi.org/10.1109/radarconf2043947.2020.9266488

Grott, M., Biele, J., Michel, P., Sugita, S., Schröder, S., Sakatani, N., et al. (2020). Macroporosity and grain density of rubble pile asteroid (162173) Ryugu. *Journal of Geophysical Research: Planets*, *125*(12), e2020JE006519. https://doi.org/10.1029/2020je006519

Hérique, A., Agnus, B., Asphaug, E., Barucci, A., Beck, P., Bellerose, J., et al. (2018). Direct observations of asteroid interior and regolith structure: Science measurement requirements. *Advances in Space Research*, *62*(8), 2141–2162. https://doi.org/10.1016/j.asr.2017.10.020

Hérique, A., Kofman, W., Beck, P., Bonal, L., Buttarazzi, I., Heggy, E., et al. (2016). Cosmochemical implications of CONSERT permittivity characterization of 67P/CG. *Monthly Notices of the Royal Astronomical Society*, *462*, S516–S532. https://doi.org/10.1093/mnras/stx040

Hérique, A., Plettemeier, D., Kofman, W., Rogez, Y., Buck, C., & Goldberg, H. (2019a). A low frequency radar to fathom asteroids from Juventas Cubesat on HERA. In *2019 EPSC-DPS joint meeting*.

Hérique, A., Plettemeier, D., Lange, C., Grundmann, J. T., Ciarletti, V., Ho, T.-M., et al. (2019b). A radar package for asteroid subsurface investigations: Implications of implementing and integration into the MASCOT nanoscale landing platform from science requirements to baseline design. *Acta Astronautica*, *156*, 317–329. https://doi.org/10.1016/j.actaastro.2018.03.058

Kofman, W., Herique, A., Barbin, Y., Barriot, J.-P., Ciarletti, V., Clifford, S., et al. (2015). Properties of the 67P/Churyumov-Gerasimenko interior revealed by CONSERT radar. *Science*, *349*. https://doi.org/10.1126/science.aab0639

Kong, J. A. (1990). *Electromagnetic wave theory*. Wiley-Interscience.

Lombardini, F., Pardini, M., Fornaro, G., Serafino, F., Verrazzani, L., Costantini, M., et al. (2009). Linear and adaptive spaceborne three-dimensional SAR tomography: A comparison on real data. *IET Radar, Sonar & Navigation*, *3*(4), 424–436. https://doi.org/10.1049/iet-rsn.2008.0171

Michel, P., Cheng, A., Küppers, M., Pravec, P., Blum, J., Delbo, M., et al. (2016). Science case for the asteroid impact mission (AIM): A component of the asteroid impact & deflection assessment (AIDA) mission. *Advances in Space Research*, *57*(12), 2529–2547. https://doi.org/10.1016/j.asr.2016.03.031

Michel, P., Kueppers, M., Sierks, H., Carnelli, I., Cheng, A. F., Mellab, K., et al. (2018). European component of the AIDA mission to a binary asteroid: Characterization and interpretation of the impact of the DART mission. *Advances in Space Research*, *62*(8), 2261–2272. https://doi.org/10.1016/j.asr.2017.12.020

Minh, D. H. T., Le Toan, T., Rocca, F., Tebaldini, S., Villard, L., Réjou-Méchain, M., et al. (2016). SAR tomography for the retrieval of forest biomass and height: Cross-validation at two tropical forest sites in French Guiana. *Remote Sensing of Environment*, *175*, 138–147. https://doi.org/10.1016/j.rse.2015.12.037

Nannini, M., & Scheiber, R. (2006). A time domain beamforming algorithm for SAR tomography. *Proc. of EUSAR-European Conference on Synthetic Aperture Radar (EUSAR)* (pp. 1–4).

Nannini, M., Scheiber, R., Horn, R., & Moreira, A. (2011). First 3-D reconstructions of targets hidden beneath foliage by means of polarimetric SAR tomography. *IEEE Geoscience and Remote Sensing Letters*, *9*(1), 60–64.

Nouvel, J. F., Herique, A., Kofman, W., & Safaeinili, A. (2005). Radar signal simulation: Surface modeling with the facet method. *Radio Science*, *39*(1), 1–17.

Nozette, S., Spudis, P., Bussey, B., Jensen, R., Raney, K., Winters, H., et al. (2010). The lunar reconnaissance orbiter miniature radio frequency (Mini-RF) technology demonstration. *Space Science Reviews*, *150*, 286–302. https://doi.org/10.1007/s11214-009-9607-5

Picardi, G., Plaut, J. J., Biccari, D., Bombaci, O., Calabrese, D., Cartacci, M., et al. (2005). Radar soundings of the subsurface of Mars. *Science*, *310*(5756), 1925–1928. https://doi.org/10.1126/science.1122165

Pursiainen, S., & Kaasalainen, M. (2016). Orbiter-to-orbiter tomography: A potential approach for small solar system bodies. *IEEE Transactions on Aerospace and Electronic Systems*, *52*(6), 2747–2759. https://doi.org/10.1109/taes.2016.150638

Reigber, A., & Moreira, A. (2000). First demonstration of airborne SAR tomography using multibaseline L-band data. *IEEE Transactions on Geoscience and Remote Sensing*, *38*(5), 2142–2152. https://doi.org/10.1109/36.868873

Sava, P., & Asphaug, E. (2018a). 3D radar wavefield tomography of comet interiors. *Advances in Space Research*, *61*(8), 2198–2213. https://doi.org/10.1016/j.asr.2018.01.040

Sava, P., & Asphaug, E. (2018b). 3D radar wavefield migration of comet interiors. *Advances in Space Research*, *62*(5), 1146–1164. https://doi.org/10.1016/j.asr.2018.06.009

Seu, R., PhillipsBiccari, R. J. D., Orosei, R., Masdea, A., Picardi, G., et al. (2007). SHARAD sounding radar on the Mars reconnaissance orbiter. *Journal of Geophysical Research*, *112*(E5). https://doi.org/10.1029/2006je002745

Soumekh, M. (1999). *Synthetic aperture radar signal processing* (p. 648). New York: Wiley.

Ulaby, F. T., Moore, R., & Fung, A. K. (1986). *Microwave remote sensing: Active and passive. Volume 3-From theory to applications*. Norwood, MA: Artech House.

Ulander, L. M., & Frolind, P. O. (1998). Ultra-wideband SAR interferometry. *IEEE Transactions on Geoscience and Remote Sensing*, *36*(5), 1540–1550. https://doi.org/10.1109/36.718858

Van den Berg, E., & Friedlander, M. P. (2008). Probing the Pareto Frontier for basis pursuit solutions. *SIAM Journal on Scientific Computing*, *31*(2), 890–912.

Van den Berg, E., & Friedlander, M. P. (2011). Sparse optimization with least-squares constraints. *SIAM Journal on Optimization*, *21*(4), 1201–1229. https://doi.org/10.1137/100785028

Walsh, K. J., & Richardson, D. C. (2008). A steady-state model of NEA binaries formed by tidal disruption of gravitational aggregates. *Icarus*, *193*(2), 553–566. https://doi.org/10.1016/j.icarus.2007.08.020

Zhu, X. X., & Bamler, R. (2010). Very high resolution spaceborne SAR tomography in urban environment. *IEEE Transactions on Geoscience and Remote Sensing*, *48*(12), 4296–4308. https://doi.org/10.1109/tgrs.2010.2050487